PHYSICAL REVIEW B **93**, 045414 (2016)

Valley depolarization dynamics and valley Hall effect of excitons in monolayer and bilayer MoS_2

T. Yu and M. W. Wu[*]

Hefei National Laboratory for Physical Sciences at Microscale, Key Laboratory of Strongly Coupled Quantum Matter Physics and Department of Physics, University of Science and Technology of China, Hefei, Anhui, 230026, China

(Received 15 September 2015; revised manuscript received 10 December 2015; published 13 January 2016)

We investigate the valley depolarization dynamics and valley Hall effect of exciton due to the electron-hole exchange interaction in mono- and bilayer MoS_2 by solving the kinetic spin Bloch equations. The effect of the exciton energy spectra by the electron-hole exchange interaction is explicitly considered. For the valley depolarization dynamics, in the monolayer MoS_2, it is found that in the strong scattering regime, the conventional motional narrowing picture in the conventional strong scattering regime is no longer valid, and a novel valley depolarization channel is opened. For the valley Hall effect of exciton, in both the mono- and bilayer MoS_2, with the exciton equally pumped in the K and K′ valleys, the system can evolve into the equilibrium state where the valley polarization is parallel to the effective magnetic field due to the exchange interaction. With the drift of this equilibrium state by applied uniaxial strain, the exchange interaction can induce the *momentum-dependent* valley/photoluminesence polarization, which leads to the valley/photoluminesence Hall current. Specifically, the disorder strength dependence of the valley Hall conductivity is revealed. In the strong scattering regime, the valley Hall conductivity decreases with the increase of the disorder strength; whereas in the weak scattering regime, it saturates to a constant, which can be much larger than the one in Fermi system due to the absence of the Pauli blocking.

DOI: 10.1103/PhysRevB.93.045414

I. INTRODUCTION

In recent years, as a new candidate to realize the valleytronics, monolayer (ML), and bilayer (BL) transition metal dichalcogenides (TMDs) have attracted much attention [1–6]. To efficiently control the valley degree of freedom in ML and BL TMDs, both the optical [2,7–19] and electrical [3,20–22] techniques have been explored. For the optical method, the chiral optical valley selection rule allows for the optical creation of the valley polarization, which is mainly realized by the excitonic excitation [2,7–19]. For the electrical method, due to the contrast Berry curvature for the electron or hole in the K and K′ valleys, the valley Hall effect of electron or hole has been predicted [3], and then confirmed by the experiments in ML [21] and BL [22] MoS_2. Furthermore, the method combining both the optical and electrical techniques to realize the valley Hall effect of trion is proposed theoretically [23]. This proposal is based on the fact that the four configurations of the trions in ML TMDs can obtain nonzero Berry curvature due to the electron-electron, hole-hole, and electron-hole (e-h) exchange interactions [23]. It can be seen that ML [2,3,7–15,20] and BL [16–19] TMDs provide an ideal platform to study the rich valley dynamics based on the valley polarization or valley current. Accordingly, on one hand, it is important to study the lifetime of the valley polarization, i.e., the valley depolarization dynamics; on the other hand, it is useful to explore efficient methods to create and control the valley current.

The valley depolarization dynamics in ML and BL TMDs has been extensively studied, showing rich features for different members [2,3,7–19]. In ML TMDs, it has been experimentally found that the steady-state valley polarization can be large (around 50%) in MoS_2, WS_2, and WSe_2 [2,12,14], whereas extremely small (around 5%) in $MoSe_2$ [11,15]. Fast valley depolarization with the lifetime about picoseconds due to the intervalley exciton transition is observed [24,25]. It is theoretically shown that due to the strong Coulomb interaction, the e-h exchange interaction [26–30] can provide an efficient valley depolarization channel based on the Maialle-Silva-Sham (MSS) mechanism [31,32]. Including the long-ranged e-h Coulomb exchange interaction including the intra- and intervalley processes derived in Ref. [26], the Hamiltonian of the exciton expressed by the center-of-mass momentum $\mathbf{k}$ is written as

$$H_{\rm ML}=\frac{\hbar^2\mathbf{k}^2}{2m_{\rm ex}}+Q(k)\begin{pmatrix}\mathbf{k}^2 & -k_+^2\\ -k_-^2 & \mathbf{k}^2\end{pmatrix}, \tag{1}$$

in which the first and second terms represent the kinetic energy and e-h exchange interaction, respectively. $m_{\rm ex}=m_e+m_h$ is the exciton mass with m_e and m_h being the electron and hole masses; $Q(k)=\frac{e^2}{2\varepsilon_0\kappa_0(|\mathbf{k}|+\kappa_{\rm sc})}|\phi_{1s}^{2D}(0)|^2\alpha_{\rm ML}$ and $k_\pm=k_x\pm ik_y$. Here, ε_0 and κ_0 stand for the vacuum permittivity and relative dielectric constant; $\kappa_{\rm sc}$ is the screening wave vector; $\phi_{1s}^{\rm 2D}(\mathbf{r})=\sqrt{8/\pi a_B^2}e^{-2r/a_B}$ represent the exciton ground-state wave function with $\mathbf{r}$ being the relative coordinate of the electron and hole, and a_B denoting the exciton radius; $\alpha_{\rm ML}$ is the material parameter [26].

This exchange interaction can cause the "precession" of the exciton states with a $\mathbf{k}$-dependent frequency $\Omega(\mathbf{k})$, which causes the inhomogeneous broadening [31,32]. In analogy to the D'yakonov-Perel' (DP) mechanism [33], in the strong scattering regime with $|\Omega(\mathbf{k})|\tau_k\ll 1$ with τ_k being the momentum relaxation time, the valley depolarization time is estimated to be $\tau_s^{-1}=\langle\Omega^2(\mathbf{k})\rangle\tau_k$. Here $\langle\cdots\rangle$ denotes the ensemble average. Accordingly, it seems that the valley depolarization should be always suppressed by the momentum scattering in the strong scattering regime. Nevertheless, Yu *et al.* showed that with the

---

[*] Author to whom correspondence should be addressed: mwwu@ustc.edu.cn

e-h exchange interaction, the energy spectra of the exciton is modified to be the Dirac cone [23]. With this large modification of the exciton spectra, the momentum scattering should also be markedly influenced by the exchange interaction. Although it is then pointed out that the Dirac cone does not exist due to the existence of the intravalley e-h exchange interaction [28–30], it is demonstrated that the exchange interaction modifies the energy spectra of the exciton markedly [28–30]. This motivates us to study the valley dynamics with the exchange interaction explicitly modifying the energy spectra.

Similar to the ML situation, in BL TMDs, the exchange interaction between the four degenerate states labeled by the valley and layer indices is also expected to cause the photoluminesence (PL) depolarization [34]. However, it is experimentally found that different from the ML situation, the steady-state PL polarization in the BL WS_2 and WSe_2 can be much larger than the one in ML under the same experimental conditions [16–19]. Then it is theoretically predicted that for the BL WS_2, with the *isotropic* dielectric constant, there exists a steady state with the PL polarization being always half of the initial one due to the specific form of the exchange interaction, indicating that the valley depolarization time can be very long in BL TMDs [34]. Specifically, the exchange interaction Hamiltonian between the four degenerate *intralayer* exciton states is written as

$$H_{\rm ex}^{\rm BL}(\mathbf{k}) \approx \tilde{Q}(k)\begin{pmatrix} \mathbf{k}^2 & \gamma k_+^2 & -k_+^2 & -\gamma\mathbf{k}^2 \\ \gamma k_-^2 & \mathbf{k}^2 & -\gamma\mathbf{k}^2 & -k_-^2 \\ -k_-^2 & -\gamma\mathbf{k}^2 & \mathbf{k}^2 & \gamma k_-^2 \\ -\gamma\mathbf{k}^2 & -k_+^2 & \gamma k_+^2 & \mathbf{k}^2 \end{pmatrix}. \quad (2)$$

Here, $\tilde{Q}(k)=\frac{e^2}{2\varepsilon_0\kappa_\parallel(|\mathbf{k}|+\kappa_{\rm sc})}|\tilde{\phi}_{1s}^{\rm 2D}(0)|^2\tilde{\alpha}_{\rm BL}$ with $\kappa_\parallel$ denoting the intralayer relative dielectric constant; $\gamma=\sqrt{\kappa_\parallel/\kappa_\perp}$ with $\kappa_\perp$ being the interlayer relative dielectric constant. The tilde labels that the parameters in the BL situation can be different from the ones in ML. Similar to the ML situation, this exchange interaction can also markedly modify the energy spectra of the exciton, which is also expected to influence the valley dynamics. Moreover, the study for the PL depolarization dynamics for the *anisotropic* dielectric constant [35] is still lacking.

From above analysis, it can be seen that by treating "valley" as "spin" in ML TMDs, the exchange interaction actually plays the role of the spin-orbit coupling (SOC) in the electronic system. In the electronic system, the intrinsic spin Hall effect has been well understood in the system with the SOC in the weak scattering limit, which is absent for the Rashba but can exist for another type of the SOC [36–45]. Moreover, it is found that the intrinsic spin Hall conductivity is a constant in the clean sample, which is nevertheless less studied in the strong scattering regime [36–45]. Then it is natural to expect that in analogy to the *intrinsic* spin Hall effect of electrons [36–45], there exists the "valley" Hall effect of exciton due to the exchange interaction in ML TMDs. Accordingly, with the generation of the exciton current, which can be realized by applying the uniaxial strain [46], the valley current perpendicular to the exciton current can emerge in ML TMDs. However, in the BL TMDs, the exchange interaction exists between *four* rather than two degenerate exciton states, which is very different from the electronic system with two degenerate spin bands. It is an interesting problem to study whether there exists the valley Hall effect of exciton for the four-state system. It is emphasized that in the previous works, the "spin" Hall effect of exciton has been proposed [47,48]. However, it is different from the proposal here. In the work of Wang *et al.* [47], the "spin" Hall effect arises due to the different strength of the SOC experienced by the electron and hole in the exciton; whereas in the work of Yao *et al.* [48], it arises from the Berry curvature, which is in analogy to the intrinsic anomalous Hall effect of the electron [49,50].

In the present work, by explicitly considering exciton energy spectra modified by the e-h exchange interaction, we investigate the valley depolarization dynamics and valley Hall effect of exciton in ML and BL MoS_2 by solving the kinetic spin Bloch equations (KSBEs) [51]. For the valley depolarization dynamics, in the ML MoS_2, it is found that with the exchange-interaction-modified energy spectra, in the strong scattering regime, the conventional relation $\tau_s \propto \tau_k^{-1}$ is no longer valid. It is shown that a novel valley depolarization channel is opened in the *strong* scattering regime, where the valley lifetime first decreases and then increases with the increase of the disorder strength, showing the Elliott-Yafet [52,53] (EY)-like behavior in the DP mechanism from the point of view of the spin relaxation [51,54–58]. This channel comes from the inhomogeneous broadening from the module of the momentum of the exciton in the exciton-disorder scattering, in which the same energy corresponds to a different momentum module with the exchange-interaction-modified energy spectra. This is very different from the conventional situation, in which the inhomogeneous broadening comes from the angular anisotropy of the momentum in the exciton-disorder scattering [31,32]. Moreover, due to the enhancement of the module-dependent inhomogeneous broadening by the momentum scattering, it shows EY-like behavior in the MSS mechanism. For the BL MoS_2, the PL depolarization dynamics with both the isotropic and anisotropic dielectric constants is investigated. With the isotropic dielectric constant, it is shown that with the exchange interaction modifying the energy spectra, the steady state revealed in our previous work [34] still exists. Whereas with the anisotropic dielectric constant, the steady state vanishes. However, it is found that when the dielectric constant is close to the isotropic situation, the PL polarization first decreases fast and then slowly, indicating that the effective depolarization time can also be much longer than the ML situation.

For the valley Hall effect of exciton, the valley Hall conductivity for the ML and BL MoS_2 in both the weak and strong scattering regimes are calculated by the KSBEs. It is shown that with the exciton in the K and K′ valleys equally pumped, the system evolves into the equilibrium state where the valley polarization is parallel to the effective magnetic field due to the exchange interaction. With the drift of this equilibrium state due to the applied uniaxial strain, this parallelism is broken and hence the effective magnetic field can induce the *momentum-dependent* out-of-plane valley/PL polarization, which accounts for the valley/PL current of exciton. Furthermore, the disorder strength dependence of the valley Hall conductivity is revealed. For both the ML and BL MoS$_2$, in the strong scattering regime, the valley Hall conductivity decreases ($\propto\tau_k^2$) with the increase of the disorder strength, whereas in the weak scattering regime, the valley Hall conductivity saturates to a constant. Specifically, it is found that the valley Hall conductivity in the weak scattering regime is proportional to the population of the exciton with zero momentum. By further considering that with the Bose distribution (therefore without the Pauli blocking), this population can be extremely large at low temperature and high exciton density. Accordingly, the valley Hall conductivity for the exciton can be much larger than the one for the Fermi system. All these behaviors can be well understood analytically in the weak exchange interaction limit.

This paper is organized as follows. In Sec. II, we set up the model and KSBEs. In Sec. III, we study the valley depolarization dynamics and valley Hall effect of exciton in ML MoS$_2$. Specifically, in Sec. III A, a novel valley depolarization channel is presented; in Sec. III B, the disorder strength dependence of the valley Hall effect of the exciton is studied first numerically and then understood analytically. In Sec. IV, the valley depolarization dynamics and valley Hall effect of the exciton are further discussed in BL MoS$_2$. We summarize in Sec. V.

II. MODEL AND KSBEs

We start the investigation from the setup of the kinetic equation for the exciton by considering the exciton-disorder scattering. We first present the effective Hamiltonian for the exciton-disorder interaction expressed by the center-of-mass coordinate of the exciton, which is derived in Refs. [59,60]. The Hamiltonian in the disordered system is written as

$$\Big[-\frac{\hbar^2}{2m_e}\nabla_e^2-\frac{\hbar^2}{2m_h}\nabla_h^2-\frac{e^2}{4\pi\varepsilon_0\kappa_0|\mathbf{r}_e-\mathbf{r}_h|}+W_e(\mathbf{r}_e) + W_h(\mathbf{r}_h)\Big]\Psi_\eta(\mathbf{r}_e,\mathbf{r}_h)=E_\eta\Psi_\eta(\mathbf{r}_e,\mathbf{r}_h), \quad (3)$$

where $W_e(\mathbf{r}_e)$ and $W_h(\mathbf{r}_h)$ denote the *intravalley* disorder potential for the electron and hole, respectively, and η labels the exciton state including the valley and layer indices. The exciton-disorder interaction can arise from the surface roughness or the interface roughness between the MoS$_2$ layer and substrate. For ML MoS$_2$, we do not consider the intervalley scattering, which is suppressed for the hole with large splitting of the valence band, because the spin-flip scattering is forbidden unless the mirror reflection symmetry is broken [26,61–63]. For BL MoS$_2$, the interlayer scattering is further neglected because only the hole with the same spin can hop between different layers, which is nevertheless very weak due to the large splitting of the valencen bands, and the interlayer hopping for the electron is forbidden due to the lattice symmetry [16–19,34]. When the disorder is not very strong, which does not influence the relative motion of the exciton, the exciton-disorder interaction can be treated perturbatively and expressed by the center-of-mass coordinate [59,60]. By focusing on the ground state (1s state), the center-of-mass part of the Hamiltonian reads

$$\Big[-\frac{\hbar^2\nabla_{\mathbf{R}}^2}{2m_{\rm ex}}+V_{\rm ex}(\mathbf{R})\Big]\Psi_{1s}(\mathbf{R})=E_{1s}\Psi_{1s}(\mathbf{R}), \quad (4)$$

where $\mathbf{R}=(m_e\mathbf{r}_e+m_h\mathbf{r}_h)/m_{\rm ex}$. Here, with $m_e\approx m_h$ in ML and BL MoS$_2$,

$$V_{\rm ex}(\mathbf{R})\approx 4\int d\mathbf{R}'\big|\phi_{1s}^{\rm 2D}(2\mathbf{R}'-2\mathbf{R})\big|^2[W_e(\mathbf{R}')+W_h(\mathbf{R}')] \quad (5)$$

describes the effective exciton-disorder interaction. From Eq. (5), one notices that the charged impurity is inefficient for the exciton-disorder interaction because $W_e(\mathbf{R}')+W_h(\mathbf{R}')=0$ for the electron and hole carrying opposite charges.

Furthermore, with the e-h exchange interaction Hamiltonian $H_{\rm ex}(\mathbf{k})$ included in Eq. (4), the exciton dynamics under the uniaxial strain can be described by the KSBEs including the coherent, drift, and scattering terms [51]:

$$\partial_t\rho_{\mathbf{k}}=\partial_t\rho_{\mathbf{k}}|_{\rm coh}+\partial_t\rho_{\mathbf{k}}|_{\rm drift}+\partial_t\rho_{\mathbf{k}}|_{\rm scat}. \quad (6)$$

In these equations, $\rho_{\mathbf{k}}$ represent the $n\times n$ density matrices of exciton with the center-of-mass momentum $\mathbf{k}$ at time t, in which the diagonal terms describe the exciton distribution functions and off-diagonal terms represent the interstate coherence. Specifically, $n=2$ and 4 for the ML and BL MoS$_2$, respectively.

In the *collinear* space, i.e., the basis of the density matrix is the exciton state labeled by the valley and layer indices [26,34], the coherent term is given by

$$\partial_t\rho_{\mathbf{k}}|_{\rm coh}=-(i/\hbar)[H_{\rm ex}(\mathbf{k}),\rho_{\mathbf{k}}], \quad (7)$$

where [,] stands for the commutator. The drift term is denoted as

$$\partial_t\rho_{\mathbf{k}}|_{\rm drift}=-(\mathbf{F}/\hbar)\cdot\nabla_{\mathbf{k}}\rho_{\mathbf{k}}, \quad (8)$$

where $\mathbf{F}$ represents the external force field due to the applied uniaxial strain. Finally, the scattering term $\partial_t\rho(\mathbf{k},t)|_{\rm scat}$ due to the exciton-disorder scattering is written as

$$\partial_t\rho_{\mathbf{k}}|_{\rm scat}=-\frac{\pi}{\hbar}\sum_{\mathbf{k}'\eta_1\eta_2}|U_{\mathbf{k}-\mathbf{k}'}|^2\delta\big(E_{\mathbf{k}',\eta_1}-E_{\mathbf{k},\eta_2}\big)\times\big[\big(T_{\mathbf{k}',\eta_1}T_{\mathbf{k},\eta_2}\rho_{\mathbf{k}}-T_{\mathbf{k},\eta_2}T_{\mathbf{k}',\eta_1}\rho_{\mathbf{k}'}\big)+\text{H.c.}\big]. \quad (9)$$

In Eq. (9),

$$|U_{\mathbf{q}}|^2=\iint d\mathbf{r}d\mathbf{r}'\langle[U(\mathbf{r})-U_0][U(\mathbf{r}')-U_0]\rangle e^{-i\mathbf{q}\cdot(\mathbf{r}-\mathbf{r}')} =\iint d\mathbf{r}d\mathbf{r}'C(\mathbf{r}-\mathbf{r}')e^{-i\mathbf{q}\cdot(\mathbf{r}-\mathbf{r}')}\equiv C_{\mathbf{q}}, \quad (10)$$

with U_0 being the average value of the disorder potential. $C(\mathbf{q})$ is taken to be the Gaussian correlation function [59,60],

$$C(\mathbf{q})=\pi V_R^2\sigma_R^2\exp\big(-\sigma_R^2q^2/4\big), \quad (11)$$

where V_R is the potential amplitude and σ_R denotes the radius of the correlation length of the disorder. Specifically, when $\sigma_Rq\ll 1$, Eq. (11) actually describes the short-range exciton-disorder interaction. $E_{\mathbf{k},\eta}$ and $T_{\mathbf{k},\eta}$ are the energy spectra of the exciton and the projection matrix, whose expressions are given explicitly in Appendix A for both the ML and BL situations.

TABLE I. Parameters used in the computation for ML MoS_2.

m_e/m_0	0.35[a]	T (K)	20
m_h/m_0	0.44[a], 0.43[b]	$n_{\rm ex}$ ($\rm cm^{-2}$)	10^{11}
κ_0	3.43[a]	$n_{\rm e}$ ($\rm cm^{-2}$)	1.6×10^{10}
a_B(nm)	3.0	σ_R (nm)	6
$\alpha_{\rm ML}$ ($\rm \mathring{A}^2$)	4.91[c]	V_{R0} (meV)	4.4×10^{-2}
F (eV/cm)	10		

[a] Reference [64].

[b] References [65,66].

[c] Reference [26].

III. MONOLAYER MoS_2

In this section, we investigate the valley depolarization dynamics and valley Hall effect for the A exciton in the ML MoS_2. All parameters including the band structure and material parameters used in our computation are listed in Table I.

In Table I, T denotes the temperature, which is low enough that the exciton-phonon interaction is neglected [59–63]; $n_{\rm ex}$ is the exciton density. According to the experiments [65,66], the ML and few-layer MoS_2 crystals are n doped. Therefore, the electron density n_e is included in our calculation, which is chosen to be much smaller than the exciton density. Accordingly, the doped electron can contribute to the screening of the Coulomb interaction [Eq. (1)], which suppresses the e-h exchange interaction. With these parameters, $\kappa_{sc} = \frac{e^2 m_e}{2\hbar^2\varepsilon_0\kappa_0}\frac{1}{e^{-\mu_e/(k_BT)}+1} \approx 1.5 \times 10^9$/m, with μ_e being the chemical potential of electron.

A. Novel valley depolarization dynamics

In this subsection, we investigate the valley depolarization dynamics, and especially focus on a novel valley depolarization channel in ML MoS_2. The valley depolarization time is obtained by solving the KSBEs from the temporal evolution of the valley polarization $P(t) = \sum_{\mathbf{k}} \mathbf{S}^z_{\mathbf{k}}(t)/n_{\rm ex} = \sum_{\mathbf{k}} {\rm Tr}[\rho_{\mathbf{k}}(t)\hat{\sigma}_z]/n_{\rm ex}$, with $\hat{\sigma}_z$ being the $\hat{z}$ component of the Pauli matrix. According to the chiral optical valley selection rule [2,9], by using the elliptically polarized light, the system is initialized to be

$$\rho_{\mathbf{k}}(0) = \frac{B_{\mathbf{k}\uparrow} + B_{\mathbf{k}\downarrow}}{2} + \frac{B_{\mathbf{k}\uparrow} - B_{\mathbf{k}\downarrow}}{2}\hat{\sigma}_z. \tag{12}$$

In Eq. (12), $B_{\mathbf{k}\sigma} = \{\exp[(\varepsilon_{\mathbf{k}} - \mu_\sigma)/(k_BT)] - 1\}^{-1}$ is the Bose-Einstein distribution function at temperature T, with $\varepsilon_{\mathbf{k}} = \hbar^2k^2/(2m_{\rm ex})$ and $\mu_{\uparrow,\downarrow}$ standing for the chemical potentials determined by the exciton density $n_{\rm ex}{=}\sum_{\mathbf{k}}{\rm Tr}[\rho_{\mathbf{k}}]$ and the initial valley polarization $P(0)$. $P(0) = 10\%$ in our numerical calculation.

1. *Analytical analysis on the conventional situation*

For comparison with the novel valley depolarization channel addressed in the next subsection (Sec. III A 2), we first present the analytical analysis of the conventional MSS mechanism [31–33], which has been used to understand the recent experimental results [13,14]. As we know, when the splitting energy due to the exchange interaction, which is referred to as the "exchange energy" in this work, is much *smaller* than the kinetic energy $\varepsilon_{\mathbf{k}}$, the exchange energy can be neglected in the energy spectra, i.e., $E_{\mathbf{k},\eta} \approx \varepsilon_{\mathbf{k}}$ in Eq. (9). Based on this approximation, Eq. (9) becomes

$$\partial_t\rho_{\mathbf{k}}|_{\rm scat} \approx -\frac{2\pi}{\hbar}\sum_{\mathbf{k}'}|U_{\mathbf{k}-\mathbf{k}'}|^2\delta(\varepsilon_{\mathbf{k}'} - \varepsilon_{\mathbf{k}})(\rho_{\mathbf{k}} - \rho_{\mathbf{k}'}). \tag{13}$$

To find the valley depolarization time, we transform the KSBEs from the collinear space to the helix one, in which the density matrix is in the basis diagonalizing the Hamiltonian Eqs. (1) and (2), by the unitary transformation $\tilde{\rho}_{\mathbf{k}} = U^\dagger_{\mathbf{k}}\rho_{\mathbf{k}}U_{\mathbf{k}}$ [67]. Here,

$$U_{\mathbf{k}} = \frac{1}{\sqrt{2}}\begin{pmatrix} -e^{2i\theta_{\mathbf{k}}} & e^{2i\theta_{\mathbf{k}}} \\ 1 & 1 \end{pmatrix}, \tag{14}$$

with $\theta_{\mathbf{k}}$ being the angle of the momentum of exciton. In the helix representation, the KSBEs become

$$\begin{aligned} &\partial_t\tilde{\rho}_{\mathbf{k}} + i\big(\varepsilon^{\rm ex}_k/\hbar\big)[\hat{\sigma}_z,\tilde{\rho}_{\mathbf{k}}] + (2\pi/\hbar)a^2\sum_{\mathbf{k}'}\delta(\varepsilon_{\mathbf{k}'} - \varepsilon_{\mathbf{k}}) \\ &\quad\times(\tilde{\rho}_{\mathbf{k}} - S_{\mathbf{k}\mathbf{k}'}\tilde{\rho}_{\mathbf{k}'}S_{\mathbf{k}'\mathbf{k}}) = 0, \end{aligned} \tag{15}$$

where the exchange energy $\varepsilon^{\rm ex}_k = Q(k)k^2$ and $S_{\mathbf{k}\mathbf{k}'} = U^\dagger_{\mathbf{k}}U_{\mathbf{k}'}$. Here, for simplicity, we consider the situation with $\sigma_R|\mathbf{k} - \mathbf{k}'| \ll 1$, hence $|U_{\mathbf{k}-\mathbf{k}'}|^2$ is replaced by the constant $a^2 = \pi V^2_R\sigma^2_R$ in Eq. (15). After Fourier analysis with $\tilde{\rho}_{\mathbf{k}} = \sum_l \tilde{\rho}^l_k e^{il\theta_{\mathbf{k}}}$, one finds that the zeroth order of the density matrix $\tilde{\rho}^0_k$ forms a closed equation,

$$\frac{\partial\tilde{\rho}^0_k}{\partial t} + \frac{i}{\hbar}\varepsilon^{\rm ex}_k\big[\hat{\sigma}_z,\tilde{\rho}^0_k\big] + \frac{\tilde{\rho}^0_k}{2\tau} - \frac{1}{2\tau}\hat{\sigma}_x\tilde{\rho}^0_k\hat{\sigma}_x = 0, \tag{16}$$

which is not obvious in the collinear representation [68]. Here, $1/\tau = m_{\rm ex}a^2/\hbar^3$ is the momentum scattering rate.

By further noticing that $\tilde{\mathbf{S}}^x_{\mathbf{k}} = \mathbf{S}^z_{\mathbf{k}}$, one obtains from Eq. (16) that

$$\begin{aligned} \mathbf{S}^z_{\mathbf{k}}(t) = {}& \frac{P(0)}{2}\left(1 + \frac{1}{\sqrt{1 - 16\Omega^2_k\tau^2}}\right)e^{(-\frac{t}{2\tau} + \frac{t}{2\tau}\sqrt{1-16\Omega^2_k\tau^2})} \\ &+ \frac{P(0)}{2}\left(1 - \frac{1}{\sqrt{1 - 16\Omega^2_k\tau^2}}\right)e^{(-\frac{t}{2\tau} - \frac{t}{2\tau}\sqrt{1-16\Omega^2_k\tau^2})}, \end{aligned} \tag{17}$$

where $\Omega_k = \varepsilon^{\rm ex}_k/\hbar$ is the precession frequency between different exciton states. Moreover, according to the conventional DP mechanism for spin relaxation [33], $2\langle\Omega_k\rangle\tau \approx 1$ labels the boundary between the weak and strong scattering regimes, because $2\Omega_k\tau \gtrsim 1$ ($2\Omega_k\tau \lesssim 1$) means that the precession angle of "spins" around the effective magnetic field due to the exchange interaction is relatively large (small) between adjacent scattering events. From Eq. (17), it is obtained that in the strong scattering limit with $\Omega_k\tau \ll 1$,

$$\mathbf{S}^z_{\mathbf{k}}(t) \approx P(0)\exp\big(-4\Omega^2_k\tau t\big), \tag{18}$$

and hence the valley depolarization time $\tau_v \approx [4\langle\Omega^2_k\rangle\tau]^{-1}$ is inversely proportional to the momentum scattering time, which is the motional narrowing effect in the random-walk theory [51,54–58]. Whereas in the weak scattering limit with

$\Omega_k \tau \gg 1$,

$$\mathbf{S}^z_{\mathbf{k}}(t) \approx P(0) e^{-t/(2\tau)} \cos(2\Omega_k t). \tag{19}$$

Hence, two factors influence the valley depolarization in the weak scattering limit. On one hand, the momentum scattering opens a valley depolarization channel due to the factor $e^{-t/(2\tau)}$; on the other hand, the factor $\cos(2\Omega_k t)$ can cause free induction decay due to different precession frequency with different momentum (inhomogeneous broadening) [51,68].

However, with the *same* initial state [Eq. (12)], the above conventional picture obtained by the weak exchange energy approximation is no longer valid when the exchange energy is comparable to or even larger than the kinetic one [26,28–30], which is shown in the next subsection.

2. *Momentum scattering dependence of the novel valley depolarization*

In ML MoS_2, due to the strong Coulomb interaction and the large exciton mass, the exchange energy is comparable to the kinetic one [26,28–30]. This is true even when the screening effect due to the residue electron in the sample is considered (Table I). Therefore, the exchange energy should enter the energy spectra in the scattering term when calculating the valley depolarization time. Consequently, a novel valley depolarization channel in the strong scattering regime, in which the valley depolarization is enhanced rather than suppressed by the momentum scattering, showing the EY-like behavior [52,53], is switched on.

To understand the new valley depolarization channel, we focus on a simplified model, where only the diagonal elements in the projection matrix [Eq. (A2)] are retained. The corresponding scattering term reads

$$\partial_t \rho_{\mathbf{k}}|_{\text{scat}} \approx -\frac{1}{4\tau} \sum_{\eta_1 \eta_2} \int d\varepsilon_{k'} \delta\big(E_{\mathbf{k}',\eta_1} - E_{\mathbf{k},\eta_2}\big)\big(\rho_{\mathbf{k}} - \rho^0_{k'}\big), \tag{20}$$

where $\rho^0_{k'} = \frac{1}{2\pi} \int d\theta_{\mathbf{k}'} \rho_{\mathbf{k}'}$. Furthermore, by means of the Fourier analysis, the density matrix is expanded as $\rho_{\mathbf{k}} = \rho^0_k + \sum_{l \neq 0} \rho^l_{\mathbf{k}} e^{il\theta_{\mathbf{k}}}$, where the zeroth and nonzeroth components are written separately. It can be seen that for the zeroth order of $\rho_{\mathbf{k}}$, the scattering term,

$$\partial_t \rho_{\mathbf{k}}|_{\text{scat}} \approx -\frac{1}{4\tau} \sum_{\eta_1 \eta_2} \int d\varepsilon_{k'} \delta\big(E_{\mathbf{k}',\eta_1} - E_{\mathbf{k},\eta_2}\big)\big(\rho^0_k - \rho^0_{k'}\big), \tag{21}$$

is nonzero for the exciton-disorder scattering between different energy branches, whereas it is forbidden in the conventional situation from Eq. (13).

Therefore, Eq. (21) opens an additional valley depolarization channel by causing the module-dependent inhomogeneous broadening. This is very different from the conventional situation, in which the inhomogeneous broadening arises from the angular anisotropy of the momentum in the exciton-disorder scattering [31,32]. With this enhancement of the inhomogeneous broadening, the valley depolarization tends to be enhanced. However, this additional channel also enhances the momentum scattering, which tends to suppress the valley depolarization. Therefore, there exists the competition between the effective inhomogeneous broadening and momentum scattering in this new channel. It is demonstrated that the EY-like behavior exactly comes from this enhancement of the inhomogeneous broadening. It is shown in Fig. 1 that compared to the full calculation (the red solid curve with circles), when the additional valley depolarization channel is removed, the EY-like behavior vanishes in the pink chain curve.

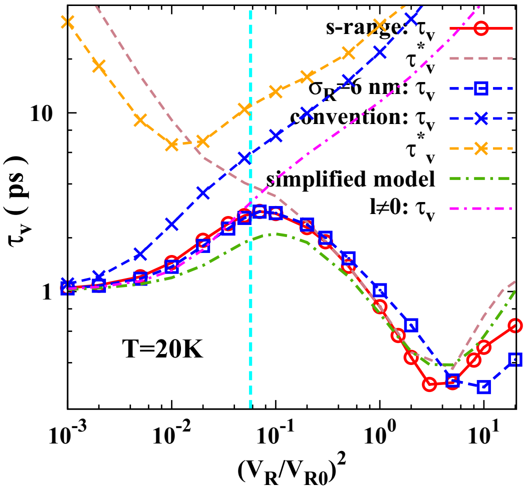

FIG. 1. Disorder strength dependence of the valley depolarization time in ML MoS_2. The boundary between the weak and strong scattering regimes $[2\langle\Omega_k\rangle\tau \approx 1]$ is denoted by the vertical cyan dashed line. The valley depolarization times with both the short-range scattering (the red solid curve with circles) and Gaussian correlation function with $\sigma_R = 6$ nm (the blue dashed curve with squares) are shown. With short-range scattering, the red solid curve with circles for τ_v and gray dashed curve for τ^*_v correspond to the valley depolarization times fitted from $\sum_{\mathbf{k}} \mathbf{S}_{\mathbf{k}}$ and $\sum_{\mathbf{k}} |\mathbf{S}_{\mathbf{k}}|$, respectively. For comparison, the conventional situation is plotted by the blue (τ_v from $\sum_{\mathbf{k}} \mathbf{S}_{\mathbf{k}}$) and orange ($\tau^*_v$ from $\sum_{\mathbf{k}} |\mathbf{S}_{\mathbf{k}}|$) dashed curve with crosses. Finally, the green chain curve corresponds to the simplified model [Eq. (20)], and the pink chain curve represents the situation with Eq. (21) removed from Eq. (9).

Figure 1 shows the disorder strength dependence of the valley depolarization time computed, based on the material parameters shown in Table I. In Fig. 1, the boundary between the weak and strong scattering regimes $[(V_R/V_{R0})^2 \approx 0.06]$ is shown as the vertical cyan dashed line. Accordingly, it is shown that with both the short-range (the red solid curve with circles) and Gaussian correlation function (the blue dashed curve with squares) in the scattering term, in the weak scattering regime, the valley depolarization time increases with the increase of the disorder strength; whereas in the strong scattering regime, the valley depolarization is first enhanced and then suppressed by the momentum scattering, which is referred to as the EY-like and normal strong scattering regimes. Furthermore, these two curves for the short-range and Gaussian correlation function coincide with each other, showing that the short-range scattering is a good approximation for the exiton-disorder scattering here. This is because for the Bose-Einstein distribution at low temperature here, $q\sigma_R \ll 1$ is satisfied, and hence the exponential function in Eq. (11) can be neglected. In this situation, the momentum scattering time with the Gaussian correlation function [Eq. (11)], i.e.,

$$\tau_k^{-1} = \frac{m_{\rm ex}a^2}{2\pi\hbar^3}\int_0^{2\pi}\exp\{-2\sigma_R^2k^2[1-\cos(\theta_{\bf k}-\theta_{{\bf k}'})]\}\times[1-\cos(\theta_{{\bf k}'})]d\theta_{{\bf k}'}, \tag{22}$$

is reduced to τ without momentum dependence.

For comparison, the conventional situation is also computed, shown by the blue dashed curve with crosses in Fig. 1. It can be seen that with the increase of the disorder strength, the valley depolarization time increases monotonically in both the weak and strong scattering regimes. In the strong scattering regime, this confirms Eq. (18) where the valley depolarization is suppressed by the momentum scattering. Whereas in the weak scattering regime, from Eq. (19), it seems that the valley depolarization should be enhanced by the momentum scattering. However, because the energy dispersion in the Bose-Einstein distribution, the free induction decay dominates the valley depolarization, which can be suppressed by the momentum scattering. To see this point, we plot the valley depolarization time τ_v^* fitted from incoherently summed spin polarization $\sum_{\bf k}|{\bf S}_{\bf k}|$ [69–72], where the free induction decay is destroyed. It is shown by the orange dashed curve with crosses that with the increase of the disorder strength, τ_v^* decreases in the weak scattering regime because the momentum scattering can directly open a channel for the valley depolarization [$e^{-t/(2\tau)}$ in Eq. (19)], but increases in the strong scattering regime.

It is interesting to see that the behavior of the valley depolarization with the exchange-interaction-modified energy spectra is similar to the conventional situation in the weak scattering regime, but very different in the strong scattering regime. In the weak scattering regime, the new valley polarization channel is not important, which can be seen from Fig. 1 that the valley depolarization with (green chain curve) and without (pink chain curve) this channel almost coincides with each other. Therefore, same as the conventional situation, due to the suppression of the free induction decay by the scattering, the valley depolarization time increases with the increase of the disorder strength. By further fitting τ_v^* from incoherently summed spin polarization $\sum_{\bf k}|{\bf S}_{\bf k}|$ (gray dashed curve), one observes τ_v^* decreases with the increase of the disorder strength in the weak scattering regime due to the destruction of the free induction decay. In the EY-like regime, the enhancement of the valley depolarization by the scattering comes from the enhancement of inhomogeneous broadening due to the novel valley depolarization channel [Eq. (21)]. Finally, to show the trend of the valley depolarization time with further increasing the scattering strength, we extend our calculation to the regime $\langle\Omega_k\rangle\tau \ll 1$, i.e., the normal strong scattering regime. In this regime, the enhancement of the momentum scattering in Eq. (21) becomes more important than the enhancement of the inhomogeneous broadening, and hence the valley depolarization is suppressed by the momentum scattering.

Finally, it can be seen from Fig. 1 that the green chain curve calculated from the simplified model [Eq. (20)] almost coincides with the one by full calculation (the red solid curve with circles). Therefore, it seems that the off-diagonal elements in the projection matrix play a less important role in the valley depolarization in the regimes we study. However, it influences the behavior of the temporal evolution of the valley polarization in the normal strong scattering regime, leading to the oscillations of the valley polarization (refer to Appendix B).

B. Valley Hall effect of exciton

In this part, we study the valley Hall effect of exciton in ML MoS$_2$ both numerically and analytically. In the calculation, the initial state is set to be the equally populated Bose-Einstein distribution in the K and K′ valleys, i.e.,

$$\rho_{\bf k}(0) = B_k^0\hat{I}, \tag{23}$$

where B_k^0 is the Bose-Einstein distribution function. The computation parameters are listed in Table I. With this experimentally realized initial state [2,9], we first show that the system can evolve to the equilibrium state in which the "spin" vectors [${\bf S}_{\bf k}^x = {\rm Tr}(\rho_{\bf k}\hat{\sigma}_x)$, ${\bf S}_{\bf k}^y = {\rm Tr}(\rho_{\bf k}\hat{\sigma}_y)$, and ${\bf S}_{\bf k}^z$] are parallel to the **k**-dependent magnetic field due to the exchange interaction [Sec. III B 1]. Then we show that with this equilibrium state, after applying the external force field due to the uniaxial strain [46,48], the drift of this equilibrium state can induce the valley Hall current of exciton (Sec. III B 2).

1. *Equilibrium state without external force field*

Before the concrete study of the valley Hall effect of the exciton in ML MoS$_2$, it is important to know the property of the equilibrium state with the exciton initially equally populated in the K and K′ valleys. In Figs. 2(a) and 2(b), it is shown that after a long time, the system evolves into the equilibrium state which corresponds to the "spin" separation for ${\bf S}_{\bf k}^x$ and ${\bf S}_{\bf k}^y$ in the momentum space, respectively. Specifically, in this equilibrium state, the spin vectors ${\bf S}_{\bf k}^x$ and ${\bf S}_{\bf k}^y$ are parallel to the **k**-dependent magnetic field due to the exchange interaction $\boldsymbol{\Omega}_{\bf k}^x = -2\varepsilon_k^{\rm ex}\cos(2\theta_{\bf k})$ and $\boldsymbol{\Omega}_{\bf k}^y = -2\varepsilon_k^{\rm ex}\sin(2\theta_{\bf k})$. Below we analytically demonstrate this property in the weak exchange interaction limit.

In the weak exchange interaction limit, we expand the energy spectra in the linear order of the exchange energy in the scattering term [Eq. (9)], and then derive the equilibrium state to be (the derivation is referred to Appendix C)

$$\rho_{\bf k}^e \approx B_k^0\hat{I} + \mathscr{H}_{\bf k}^{\rm ex}\partial B_k^0/\partial\varepsilon_k. \tag{24}$$

Here, with the diagonal elements contributing to the energy spectra, the exchange interaction Hamiltonian,

$$\mathscr{H}_{\bf k}^{\rm ex} = \varepsilon_k^{\rm ex}\begin{pmatrix} 0 & -e^{2i\theta_{\bf k}} \\ -e^{-2i\theta_{\bf k}} & 0 \end{pmatrix}, \tag{25}$$

only contains the off-diagonal elements. This equilibrium state corresponds to the spin vectors,

$$S_{\bf k}^x = -2\varepsilon_k^{\rm ex}\cos(2\theta_{\bf k})\partial B_k^0/\partial\varepsilon_k, \tag{26}$$

$$S_{\bf k}^y = -2\varepsilon_k^{\rm ex}\sin(2\theta_{\bf k})\partial B_k^0/\partial\varepsilon_k. \tag{27}$$

Obviously, the spin vectors $S_{\bf k}^x$ and $S_{\bf k}^y$ are parallel to the **k**-dependent magnetic field $\boldsymbol{\Omega}_{\bf k}^x$ and $\boldsymbol{\Omega}_{\bf k}^y$, respectively.

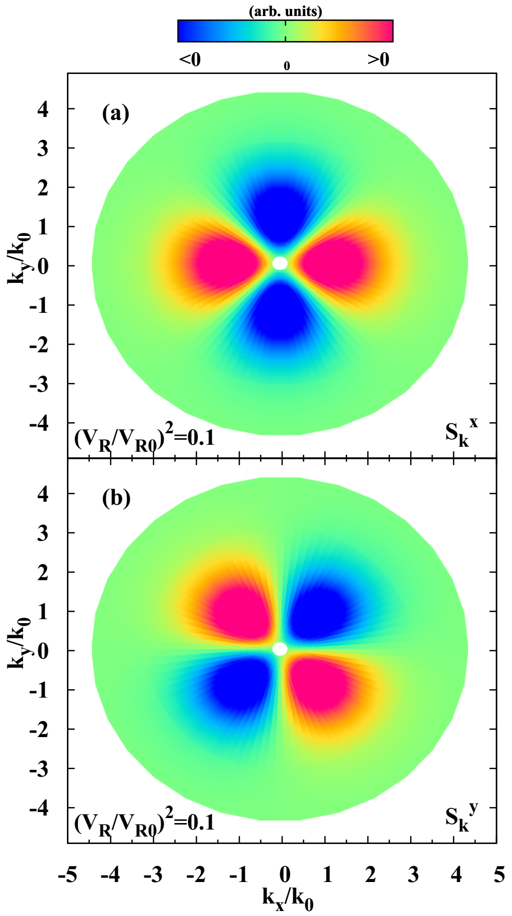

FIG. 2. Momentum distribution of the "spin" vectors $\mathbf{S}_{\mathbf{k}}^x$ (a) and $\mathbf{S}_{\mathbf{k}}^y$ (b) in the equilibrium state. $k_0 \approx 7.9 \times 10^7$/m is the Fermi wave vector of the system. The calculation shows that in the equilibrium state, $\mathbf{S}_{\mathbf{k}}^x \propto \cos(2\theta_{\mathbf{k}})$ and $\mathbf{S}_{\mathbf{k}}^y \propto \sin(2\theta_{\mathbf{k}})$, which are parallel to the in-plane effective magnetic field due to the exchange interaction along the $\hat{x}$ direction $[\mathbf{\Omega}_{\mathbf{k}}^x = -2\varepsilon_k^{\rm ex}\cos(2\theta_{\mathbf{k}})]$ and $\hat{y}$ direction $[\mathbf{\Omega}_{\mathbf{k}}^y = -2\varepsilon_k^{\rm ex}\sin(2\theta_{\mathbf{k}})]$, respectively.

2. *Valley Hall effect of exciton*

In this subsection, we study the valley Hall effect of exciton. Specifically, we explicitly show the disorder strength (momentum scattering) dependence of the valley Hall conductivity σ_x^z. From the initial state Eq. (23), we numerically calculate the steady-state density matrix with the applied field after a long temporal evolution by the KSBEs. Then the valley Hall conductivity is calculated. With the valley Hall current defined as

$$j_x^z = \sum_{\mathbf{k}} \mathrm{Tr}\left[\rho_{\mathbf{k}}\frac{1}{2}(\hat{\sigma}_z\hat{v}_y + \hat{v}_y\hat{\sigma}_z)\right] = \sigma_x^z F/|e|, \tag{28}$$

the valley Hall conductivity σ_x^z is expressed as

$$\sigma_x^z = \frac{|e|}{2F}\sum_{\mathbf{k}} \mathrm{Tr}[\rho_{\mathbf{k}}(\hat{\sigma}_z\hat{v}_y + \hat{v}_y\hat{\sigma}_z)]. \tag{29}$$

Here, $|e|$ is the electron charge and $\hat{v}_y = \hbar k_y/m_{\rm ex} + \partial H_{\rm ex}^{\rm ML}(\mathbf{k})/\partial k_y$ is the velocity operator.

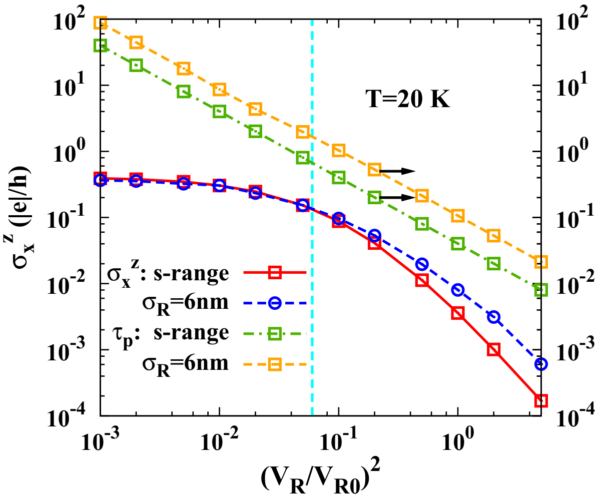

FIG. 3. Disorder strength dependence of the valley Hall conductivity and the momentum scattering time (note the scale is on the right-hand side of the frame). The cyan dashed line labels the boundary between the weak and strong scattering regimes. The green chain (short-range) and orange dashed (Gaussian correlation) curves with squares show that the momentum scattering time is linearly dependent on the disorder strength. For the valley Hall conductivity, it can be seen from the red solid curve with squares (short-range) and blue dashed curve with circles (Gaussian correlation) that in the strong scattering limit, the valley Hall conductivity decreases with the increase of the disorder strength with the dependence $\sigma_x^z \propto \tau^2$, whereas in the weak scattering regime, the valley Hall conductivity saturates to a constant.

The results are shown in Fig. 3. With the weak external force field, the system is in the linear regime, as shown in Fig. 3, and the momentum scattering time reveals linear dependence on the disorder strength. In this regime, it can be seen from Fig. 3 that in the strong scattering regime, the valley Hall conductivity decreases with the increase of the disorder strength, showing the dependence $\sigma_x^z \propto \tau^2$, whereas in the weak scattering regime, the valley Hall conductivity saturates to a constant. Below we show analytically that these features in the momentum scattering dependence can be well understood in the weak exchange interaction approximation.

Here, we outline the main results to obtain the physical picture of the valley Hall effect of the exciton. It has been shown that without the external force field, the density matrix in the equilibrium state is written as Eq. (24), which commutes with the exchange interaction Hamiltonian. After applying the external force field, the density matrix in the steady state is derived in Appendix D, as shown by Eq. (D5). It is shown that based on the equilibrium state [Eq. (24)], after applying the external field, the drift part of the density matrix is [Eq. (D2)]

$$\rho_{\mathbf{k}}^{(1)} = -\frac{F\tau}{\hbar}\frac{\partial}{\partial k_x}\left(B_k^0\hat{I} + \mathscr{H}_{\mathbf{k}}^{\rm ex}\frac{\partial B_k^0}{\partial \varepsilon_k}\right). \tag{30}$$

Obviously, this drift density matrix no longer commutes with the exchange interaction Hamiltonian, i.e., it can induce the momentum-dependent "spin" polarization along the $\hat{z}$ direction (valley polarization). This can be seen as follows. In Eq. (D5), the induced density matrix responsible for the valley polarization is written as

$$\rho_{\mathbf{k}}^{\rm in} \approx \frac{i}{\hbar^2} F \frac{\partial B_k^0}{\partial \varepsilon_k} \frac{\tau^2}{1+4\Omega_k^2\tau^2}\left[\mathscr{H}_{\mathbf{k}}^{\rm ex}, \frac{\partial \mathscr{H}_{\mathbf{k}}^{\rm ex}}{\partial k_x}\right]. \tag{31}$$

Then with the exchange interaction Hamiltonian [Eq. (25)], it can be obtained that

$$\partial \mathscr{H}_{\mathbf{k}}^{\rm ex}/\partial k_x \approx -2Qk_x\hat{\sigma}_x + 2Qk_y\hat{\sigma}_y; \tag{32}$$

$$\left[\mathscr{H}_{\mathbf{k}}^{\rm ex}, \partial \mathscr{H}_{\mathbf{k}}^{\rm ex}/\partial k_x\right] \approx 4iQ^2k^2k_y\hat{\sigma}_z. \tag{33}$$

In the derivation, we have used the fact that when the screening effect due to the residue electron is considered, $Q(k)$ is approximately a constant with our computation parameters (Table I). From Eq. (33), one observes that the induced density matrix is proportional to $\hat{\sigma}_z$ and dependent on the momentum k_y.

Then the valley Hall conductivity can be calculated. With the definition of the valley Hall conductivity [Eq. (29)], only the third term on the right-hand side of Eq. (D5), i.e., Eq. (31), contributes to the valley Hall conductivity. From Eq. (29), one has

$$\sigma_x^z = -\frac{|e|}{h}\int_0^\infty d\varepsilon_k \frac{dB_k^0}{d\varepsilon_k}\frac{4\Omega_k^2\tau^2}{1+4\Omega_k^2\tau^2}. \tag{34}$$

From the above equation, one finds that in the strong scattering regime, with $\Omega_k\tau \ll 1$,

$$\sigma_x^z \approx -\frac{4|e|}{h}\int_0^\infty d\varepsilon_k \frac{dB_k^0}{d\varepsilon_k}\Omega_k^2\tau^2, \tag{35}$$

which is proportional to τ^2. Whereas in the weak scattering regime with $\Omega_k\tau \gtrsim 1$,

$$\sigma_x^z \approx \frac{|e|}{h}B_{k=0}^0, \tag{36}$$

which is independent on the exchange interaction strength and momentum scattering. Specifically, one observes that σ_x^z is proportional to $B_{k=0}^0$, which can be extremely large when the system is close to the Bose-Einstein condensation. Here, with the computation parameters (Table I), $B_{k=0}^0 \approx 0.6$, and hence $\sigma_x^z \approx 0.6|e|/h$, which gives a good estimate to the calculated one $0.4|e|/h$ with strong exchange interaction. Moreover, from Eq. (36), one observes that with the higher exciton density and/or lower temperature, $B_{k=0}^0$ is large and hence the valley Hall conductivity. According to our calculation, with the exciton density $n_{\rm ex} = 5 \times 10^{11}$ cm^{-2} at 10 K, $\sigma_x^z \approx 5.5|e|/h$ in the weak scattering limit. This is much larger than the one in the Fermi system, with the latter being limited by the Pauli blocking [43,44].

Finally, we summarize the physical picture of the valley Hall effect of the exciton as follows. First of all, it is understood that in the equilibrium state, the "spin" vector of any momentum $\mathbf{k}$ is parallel to the $\mathbf{k}$-dependent effective magnetic field due to the e-h exchange interaction (Sec. III B 1). Then by applying the force field due to the uniaxial strain [46], the "spin" vector is no longer parallel to the effective magnetic field. Accordingly, the "spin" vector can rotate around the effective magnetic field, and the *momentum-dependent* valley polarization is induced. Specifically, for the exciton with opposite k_y, the $\hat{x}$ component of the effective magnetic field is along the opposite direction, and hence the induced valley polarization is also opposite. Consequently, the valley current perpendicular to the driven exciton current is established.

It is emphasized that the physical picture addressed above is in analogy to the intrinsic spin Hall effect of the electron [36,43–45]. Nevertheless, two new features in this mechanism are further revealed here. On one hand, it is revealed that in the dirty sample corresponding to the strong scattering regime, the intrinsic "spin" Hall effect is markedly suppressed by the momentum scattering, with its conductivity proportional to τ^2. On the other hand, in the weak scattering regime, the Bose system with no Pauli blocking provides an ideal platform to realize large "spin" Hall conductivity, which can be much larger than the one in the Fermi system, especially when the system is close to the Bose-Einstein condensation.

IV. BILAYER MoS$_2$

In this section, we investigate the valley depolarization dynamics and valley Hall effect for the *A* exciton, which is fourfold degenerate, in BL MoS$_2$. In our previous work, a steady state in the PL depolarization dynamics in BL WS$_2$ with the isotropic dielectric constant was revealed in the situation without the energy spectra modified by the exchange interaction [34]. However, with the exchange-interaction-modified energy spectra, as revealed in ML MoS$_2$ (Sec. III), the valley dynamics becomes very different from the conventional situation and the valley Hall effect of exciton can arise. So far, the PL depolarization dynamics for BL TMDs with the anisotropic dielectric constant is still lacking. These motivate us to calculate the related PL dynamics for the fourfold-degenerate states in the BL system with the energy spectra modified by the exchange interaction. All parameters including the band structure and material parameters used in our computation are listed in Table II.

It is emphasized that in BL TMDs, the centro-inversion symmetry exists [16–19,21,22]. Hence, no valley polarization but the PL polarization can be created by the chiral optical valley selection rule [16–19]. Similarly, no valley current but the PL current can be created by the valley Hall effect due to the symmetry, which can be measured at the edges of the device channel in the experiment [21,22].

A. PL depolarization dynamics

In this part, we focus on the new feature of the PL depolarization dynamics arising in the BL system compared to

TABLE II. Parameters used in the computation for BL MoS$_2$.

m_e/m_0	0.39[a]	T (K)	20
m_h/m_0	0.47[a,b]	$n_{\rm ex}$ (cm^{-2})	10^{11}
$\kappa_\parallel$	4.8[c]	$n_{\rm e}$ (cm^{-2})	3.3×10^{10}
a_B(nm)	3.0	σ_R (nm)	6
$\alpha_{\rm BL}$ (Å^2)	4.51[d]	V_{R0} (meV)	5.4×10^{-2}
F (eV/cm)	10		

[a] Reference [64].
[b] References [65,66].
[c] Reference [35].
[d] Reference [34].

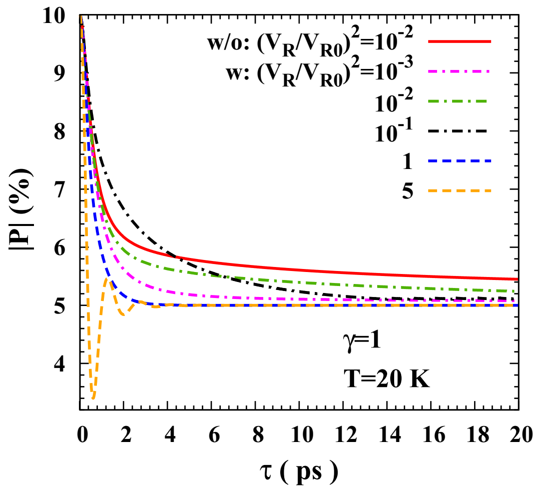

FIG. 4. Temporal evolution of the PL polarization in the BL MoS$_2$ with isotropic dielectric constant ($\gamma = 1$) and different disorder strength. It is shown that no matter the disorder strength is weak or strong, there is always a steady state with the PL polarization being half of the initial one. The red solid curve is calculated without the exchange-interaction-modified energy spectra [34].

the ML situation. The PL depolarization dynamics is obtained by solving the KSBEs from the temporal evolution of the PL polarization $P(t) = \sum_{\mathbf{k}} \mathrm{Tr}[\rho_{\mathbf{k}}(t)\hat{I}_z]/n_{\mathrm{ex}}$ with

$$\hat{I}_z = \begin{pmatrix} 1 & 0 & 0 & 0 \\ 0 & -1 & 0 & 0 \\ 0 & 0 & -1 & 0 \\ 0 & 0 & 0 & 1 \end{pmatrix}. \tag{37}$$

In the calculation, the initial condition is set to be

$$\rho_{\mathbf{k}}(0) = \frac{B_{\mathbf{k}\uparrow} + B_{\mathbf{k}\downarrow}}{2} + \frac{B_{\mathbf{k}\uparrow} - B_{\mathbf{k}\downarrow}}{2}\hat{I}_z. \tag{38}$$

$P(0)$ is set to be 10% in our numerical calculation. Below, the PL depolarization dynamics with isotropic and anisotropic dielectric constants are investigated, respectively.

For the isotropic dielectric constant ($\gamma = 1$), it is shown in Fig. 4 that no matter the system lies in the weak or strong scattering regime, there is always a steady state with the PL polarization being half of the initial one. This is the same as our previous prediction without the exchange-interaction-modified energy spectra (the red solid curve in Fig. 4) [34]. However, when the exchange interaction markedly modifies the energy spectra, the density matrix in the steady state is found to be different from the previous one [34].

In our previous work, with the initial condition Eq. (38), when the system lies in the steady state, the density matrix is found to be [34]

$$\rho^s_{\mathbf{k}} = \frac{B_{\mathbf{k}\uparrow} + B_{\mathbf{k}\downarrow}}{2} + \frac{B_{\mathbf{k}\uparrow} - B_{\mathbf{k}\downarrow}}{4}\begin{pmatrix} 1 & 0 & 0 & 1 \\ 0 & -1 & -1 & 0 \\ 0 & -1 & -1 & 0 \\ 1 & 0 & 0 & 1 \end{pmatrix}. \tag{39}$$

Here, with the exchange interaction markedly modifying the energy spectra, the form of the density matrix in the steady state is different, in which no zero elements arise and hence all states are correlated to each other. This can be understood in the weak exchange interaction approximation. As a simplified model, with the diagonal and off-diagonal elements entering the energy spectra of the exciton, the effective exchange interaction in BL MoS$_2$ is written as

$$\tilde{\mathscr{H}}^{\mathrm{ex}}_{\mathbf{k}} \approx \tilde{\varepsilon}^{\mathrm{ex}}_{k}\begin{pmatrix} 0 & \gamma e^{2i\theta_{\mathbf{k}}} & -e^{2i\theta_{\mathbf{k}}} & 0 \\ \gamma e^{-2i\theta_{\mathbf{k}}} & 0 & 0 & -e^{-2i\theta_{\mathbf{k}}} \\ -e^{-2i\theta_{\mathbf{k}}} & 0 & 0 & \gamma e^{-2i\theta_{\mathbf{k}}} \\ 0 & -e^{2i\theta_{\mathbf{k}}} & \gamma e^{2i\theta_{\mathbf{k}}} & 0 \end{pmatrix}, \tag{40}$$

where $\tilde{\varepsilon}^{\mathrm{ex}}_{k} = \tilde{Q}(k)k^2$. In the weak exchange interaction approximation, the KSBEs for the BL MoS$_2$ are similar to the ML situation (Appendixes C and D),

$$\frac{\partial \rho_{\mathbf{k}}}{\partial t} + \frac{F}{\hbar}\frac{\partial \rho_{\mathbf{k}}}{\partial k_x} + \frac{i}{\hbar}\big[\tilde{\mathscr{H}}^{\mathrm{ex}}_{\mathbf{k}},\rho_{\mathbf{k}}\big] + \frac{\rho_{\mathbf{k}} - \rho^0_k}{\tau} - \frac{\pi}{\tau}\int \frac{d\theta_{\mathbf{k}'}}{(2\pi)^2}$$
$$\times\, d\delta(\varepsilon_{k'} - \varepsilon_k)\big\{\tilde{\mathscr{H}}^{\mathrm{ex}}_{\mathbf{k}} - \tilde{\mathscr{H}}^{\mathrm{ex}}_{\mathbf{k}'},\rho_{\mathbf{k}} - \rho_{\mathbf{k}'}\big\} = 0, \tag{41}$$

where {,} denotes the anticommutator. Without the applied field, in the steady state, the first three terms in the left-hand side of Eq. (41) are zero. Based on the conventional density matrix in the steady state [Eq. (39)] and following the iteration technique introduced in Appendix C, one obtains the steady state here ($\gamma = 1$),

$$\begin{aligned}\tilde{\rho}^s_{\mathbf{k}} &\approx \rho^s_{\mathbf{k}} + (1/2)\big\{\tilde{\mathscr{H}}^{\mathrm{ex}}_{\mathbf{k}},\partial\rho^s_{\mathbf{k}}/\partial\varepsilon_k\big\} \\ &= \rho^s_{\mathbf{k}} + (1/2)\tilde{\mathscr{H}}^{\mathrm{ex}}_{\mathbf{k}}(\partial B_{\mathbf{k}\uparrow}/\partial\varepsilon_{\mathbf{k}} + \partial B_{\mathbf{k}\downarrow}/\partial\varepsilon_{\mathbf{k}}).\end{aligned} \tag{42}$$

Obviously, Eq. (42) commutes with the exchange interaction Hamiltonian Eq. (40). Specifically, due to $\tilde{\mathscr{H}}^{\mathrm{ex}}_{\mathbf{k}}$ in Eq. (42), all states become correlated to each other.

For the anisotropic dielectric constant, it is seen from Fig. 5 that compared to the isotropic case $\gamma = 1$, when the dielectric constant is tuned to be anisotropic with $\gamma = 1.1$ (the blue

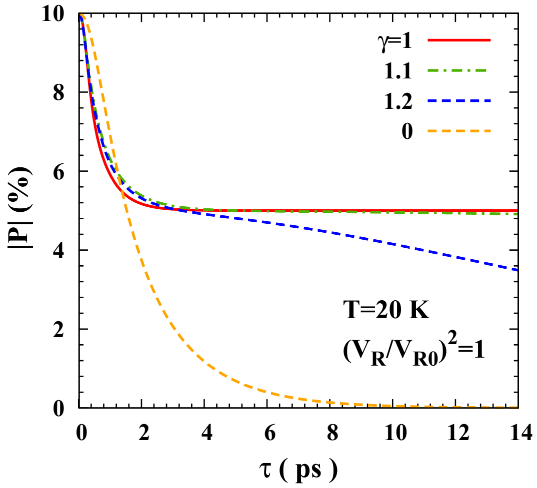

FIG. 5. Temporal evolution of the PL polarization in the BL MoS$_2$ with anisotropic dielectric constant. When the dielectric constant is tuned to be anisotropic with $\gamma = 1.1$ (the blue chain curve) and 1.2 (the green dashed curve), the steady state vanishes. For comparison, the time evolution of the valley polarization in ML MoS$_2$ is also plotted, which is shown as $\gamma = 0$ by the orange dashed curve.

chain curve) and 1.2 (the green dashed curve), the steady state vanishes.

However, when γ is close to the isotropic situation, the PL polarization first decreases fast and then slowly. Accordingly, the effective depolarization time can also be much longer than the ML situation, shown as $\gamma = 0$ by the orange dashed curve.

B. Valley Hall effect of exciton

In this subsection, we investigate the valley Hall effect of the exciton in BL MoS$_2$. In the calculation, the initial state is set to be the equally populated Bose-Einstein distribution in the K and K$'$ valleys in both the upper and lower layers, i.e.,

$$\rho_{\mathbf{k}}(0) = B_k^0 \hat{I}_{4\times 4}. \tag{43}$$

From the KSBEs, with the applied force field, the steady-state density matrix is calculated and then used to calculate the valley Hall conductivity. In analogy to the ML situation, with the PL current which carries the PL polarization defined as

$$\tilde{j}_x^z = \sum_{\mathbf{k}} \mathrm{Tr}\left[\rho_{\mathbf{k}} \frac{1}{2}(\hat{I}_z \hat{v}_y + \hat{v}_y \hat{I}_z)\right] = \tilde{\sigma}_x^z F/|e|, \tag{44}$$

the valley Hall conductivity $\tilde{\sigma}_x^z$ in BL MoS$_2$ is expressed as

$$\tilde{\sigma}_x^z = \frac{|e|}{2F} \sum_{\mathbf{k}} \mathrm{Tr}[\rho_{\mathbf{k}}(\hat{I}_z \hat{v}_y + \hat{v}_y \hat{I}_z)]. \tag{45}$$

Here, $\hat{v}_y = \hbar k_y/\tilde{m}_{\rm ex} + \partial H_{\rm ex}^{\rm BL}(\mathbf{k})/\partial k_y$. The calculated results with both the isotropic and anisotropic dielectric constants are summarized in Fig. 6.

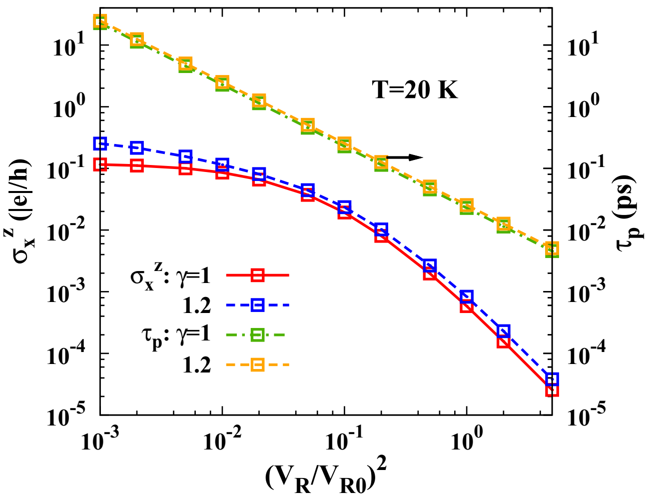

FIG. 6. Disorder strength dependence of the valley Hall conductivity in BL MoS$_2$. The blue chain ($\gamma = 1$) and orange dashed ($\gamma = 1.2$) curves with squares represent the momentum scattering time, showing the system lies in the linear regime with the applied field (note the scale is on the right-hand side of the frame). It is shown that no matter the dielectric constant is isotropic with $\gamma = 1$ (the red solid curve with squares) or anisotropic with $\gamma = 1.2$ (the blue dashed curve with squares), in the strong scattering regime, the valley Hall conductivity decreases with the increase of the disorder strength, showing the dependence $\tilde{\sigma}_x^z \propto \tau^2$, whereas in the weak scattering regime, the valley Hall conductivity saturates to a constant.

In Fig. 6, the disorder strength dependence of the valley Hall conductivity and momentum scattering time is plotted. The curves for the momentum scattering time show that the system lies in the linear regime. It can be seen from Fig. 6 that in this regime, no matter the dielectric constant is isotropic with $\gamma = 1$ (the red solid curve with squares) or anisotropic with $\gamma = 1.2$ (the blue dashed curve with squares), in the strong scattering regime, the valley Hall conductivity decreases with the increase of the disorder strength, showing the dependence $\tilde{\sigma}_x^z \propto \tau^2$, whereas in the weak scattering regime, the valley Hall conductivity saturates to a constant. This shows that although the PL depolarization dynamics in the BL MoS$_2$ is different from the ML situation, the properties of the valley Hall conductivity between them are similar. Below, the valley Hall conductivity is also derived in the weak exchange interaction approximation, with the steady-state density matrix with the applied field derived in Appendix D.

As a simplified model, the exchange interaction Hamiltonian Eq. (40) is used. From Eq. (45), it can be seen that only the third term on the left-hand side of Eq. (D5) contributes to the valley Hall conductivity. In Eq. (D5), with the exchange interaction Eq. (40), one finds

$$\begin{aligned}&\left[\tilde{\mathscr{H}}_{\mathbf{k}}^{\rm ex}, \partial \tilde{\mathscr{H}}_{\mathbf{k}}^{\rm ex}/\partial k_x\right]\\ &\approx 4i\tilde{Q}^2 k^2 k_y\\ &\times \begin{pmatrix} (\gamma^2+1) & 0 & 0 & -2\gamma \\ 0 & -(\gamma^2+1) & 2\gamma & 0 \\ 0 & 2\gamma & -(\gamma^2+1) & 0 \\ -2\gamma & 0 & 0 & (\gamma^2+1) \end{pmatrix}.\end{aligned} \tag{46}$$

It is noted that here when the screening effect is considered, $\tilde{Q}(k)$ has been treated as a constant. Accordingly, the valley Hall conductivity in BL MoS$_2$ is written as

$$\tilde{\sigma}_x^z = -2(\gamma^2+1)\frac{|e|}{h}\int_0^\infty d\varepsilon_k \frac{dB_k^0}{d\varepsilon_k}\frac{4\tilde{\Omega}_k^2\tau^2}{1+4\tilde{\Omega}_k^2\tau^2}, \tag{47}$$

where $\tilde{\Omega}_k = \tilde{\varepsilon}_k^{\rm ex}/\hbar$. Obviously, for the valley Hall conductivity in BL MoS$_2$, it is interesting to see that Eq. (47) is similar to Eq. (34) in ML MoS$_2$. Therefore, in the weak and strong scattering regimes, similar features for the valley Hall conductivity to the one in ML situation can be obtained, as addressed in Sec. III B 2.

V. SUMMARY

In summary, we have investigated the valley depolarization dynamics and valley Hall effect of the exciton in ML and BL MoS$_2$ by solving the KSBEs [51]. The effect of the exchange-interaction-modified energy spectra is explicitly considered. For the valley depolarization dynamics, in ML MoS$_2$, it is interesting to find that the conventional motional narrowing relation $\tau_s \propto \tau_k^{-1}$ in the strong scattering regime is no longer valid. It is revealed that in this regime, a novel valley depolarization channel is opened, where the valley lifetime first decreases and then increases with the increase of the disorder strength, showing the EY-like [52,53] behavior from the point view of the spin relaxation [54–58]. This channel comes from the newly module-dependent inhomogeneous broadening in the exciton-disorder scattering, in which the same energy corresponds to different momentum modules due to the exchange-interaction-modified energy spectra. This is very different from the conventional situation, in which the inhomogeneous broadening comes from the angular anisotropy of the momentum in the exciton-disorder scattering [31,32]. Moreover, due to the enhancement of the inhomogeneous broadening by this channel, EY-like behavior arises in the MSS mechanism.

For BL MoS$_2$, the PL depolarization dynamics with both the isotropic and anisotropic dielectric constants is investigated, which are found very different from the ML situation. With the isotropic dielectric constant, it is shown that with the exchange-interaction-modified energy spectra, the steady state revealed in our previous work [34] still exists. Whereas with the anisotropic dielectric constant, the steady state vanishes. However, it is found that when the dielectric constant is close to the isotropic situation, the PL polarization first decreases fast and then slowly, indicating that the effective depolarization time can be much longer than the ML situation.

For the valley Hall effect of exciton, the valley Hall conductivity for ML and BL MoS$_2$ in both the weak and strong scattering regimes are studied numerically and analytically. We show that with the exciton equally pumped in the K and K′ valleys, the exciton states evolve into the equilibrium state with the valley polarization parallel to the momentum-dependent effective magnetic field due to the exchange interaction. Then with the drift of this equilibrium state due to the applied uniaxial strain, this parallelism is broken and hence the effective magnetic field can induce the momentum-dependent valley/PL polarization, which accounts for the valley/PL current. This mechanism is in analogy to the intrinsic spin Hall effect of the electron [36,43–45].

Furthermore, it is found that although the valley/PL depolarization dynamics is very different between the ML and BL situations, the valley Hall effect shows similar features in the momentum scattering dependence. Specifically, in the strong scattering regime, the valley Hall conductivity decreases with the increase of the disorder strength ($\propto \tau^2$); whereas in the weak scattering regime, the valley Hall conductivity saturates to a constant, which is proportional to the population of the exciton with $k = 0$. Therefore, on one hand, in the dirty sample corresponding to the strong scattering regime, the valley Hall effect is markedly suppressed by the momentum scattering; on the other hand, in the weak scattering regime, the Bose system with no Pauli blocking provides an ideal platform to realize large "spin" Hall conductivity, which can be much *larger* than the one in the Fermi system, especially when the system is close to the Bose-Einstein condensation.

ACKNOWLEDGMENTS

This work was supported by the National Natural Science Foundation of China under Grants No. 11334014 and No. 61411136001, the National Basic Research Program of China under Grant No. 2012CB922002, and the Strategic Priority Research Program of the Chinese Academy of Sciences under Grant No. XDB01000000.

APPENDIX A: ENERGY SPECTRA AND PROJECTION MATRIX

In this Appendix, we present the energy spectra and projection matrix for ML and BL MoS$_2$. The derivation of the projection matrix is given in Refs. [51,67,73]. For the ML situation, the energy spectra read

$$E^{\mathrm{ML}}_{\mathbf{k},\pm} = \hbar^2k^2/(2m_{\mathrm{ex}}) + Q(k)k^2 \pm Q(k)k^2. \qquad \text{(A1)}$$

The projection matrices are

$$T^{\mathrm{ML}}_{\mathbf{k},\pm} = \frac{1}{2k^2}\begin{pmatrix} k^2 & \mp k_+^2 \\ \mp k_-^2 & k^2 \end{pmatrix}. \qquad \text{(A2)}$$

For the BL situation, the energy spectra are

$$\begin{aligned} E^{\mathrm{BL}}_{\mathbf{k},1} &= E^{\mathrm{BL}}_{\mathbf{k},2} = \hbar^2k^2/(2\tilde{m}_{\mathrm{ex}}), \\ E^{\mathrm{BL}}_{\mathbf{k},3} &= \hbar^2k^2/(2\tilde{m}_{\mathrm{ex}}) + 2(1-\gamma)\tilde{Q}(k)k^2, \\ E^{\mathrm{BL}}_{\mathbf{k},4} &= \hbar^2k^2/(2\tilde{m}_{\mathrm{ex}}) + 2(1+\gamma)\tilde{Q}(k)k^2. \end{aligned} \qquad \text{(A3)}$$

The corresponding projection matrices are given by

$$T^{\mathrm{BL}}_{\mathbf{k},1} = \frac{1}{2k^2}\begin{pmatrix} 0 & 0 & 0 & 0 \\ 0 & k^2 & 0 & k_-^2 \\ 0 & 0 & 0 & 0 \\ 0 & k_+^2 & 0 & k^2 \end{pmatrix}, \qquad \text{(A4)}$$

$$T^{\mathrm{BL}}_{\mathbf{k},2} = \frac{1}{2k^2}\begin{pmatrix} k^2 & 0 & k_+^2 & 0 \\ 0 & 0 & 0 & 0 \\ k_-^2 & 0 & k^2 & 0 \\ 0 & 0 & 0 & 0 \end{pmatrix}, \qquad \text{(A5)}$$

$$T^{\mathrm{BL}}_{\mathbf{k},3} = \frac{1}{4k^2}\begin{pmatrix} k^2 & -k_+^2 & -k_+^2 & k^2 \\ -k_-^2 & k^2 & k^2 & -k_-^2 \\ -k_-^2 & k^2 & k^2 & -k_-^2 \\ k^2 & -k_+^2 & -k_+^2 & k^2 \end{pmatrix}, \qquad \text{(A6)}$$

and

$$T^{\mathrm{BL}}_{\mathbf{k},4} = \frac{1}{4k^2}\begin{pmatrix} k^2 & k_+^2 & -k_+^2 & -k^2 \\ k_-^2 & k^2 & -k^2 & -k_-^2 \\ -k_-^2 & -k^2 & k^2 & k_-^2 \\ -k^2 & -k_+^2 & k_+^2 & k^2 \end{pmatrix}. \qquad \text{(A7)}$$

APPENDIX B: ROLE OF OFF-DIAGONAL ELEMENTS OF EQ. (A2) ON VALLEY DEPOLARIZATION

Here, we address the role of the off-diagonal elements in the projection matrix [Eq. (A2)] on the temporal evolution of valley polarization in ML MoS$_2$. It is shown in Fig. 7 by the dashed curves that without the off-diagonal elements in the projection matrix, the valley depolarization is a little enhanced compared to the full calculation by the solid curves in the weak scattering [$(V/V_{R0})^2 = 0.01$], EY-like [$(V/V_{R0})^2 = 0.5$], and normal strong scattering [$(V/V_{R0})^2 = 10$] regimes. Moreover, in the normal strong scattering regime, the off-diagonal elements of Eq. (A2) cause the oscillations in the temporal evolution of the valley polarization, shown as the black solid curve. By removing the off-diagonal elements in the projection

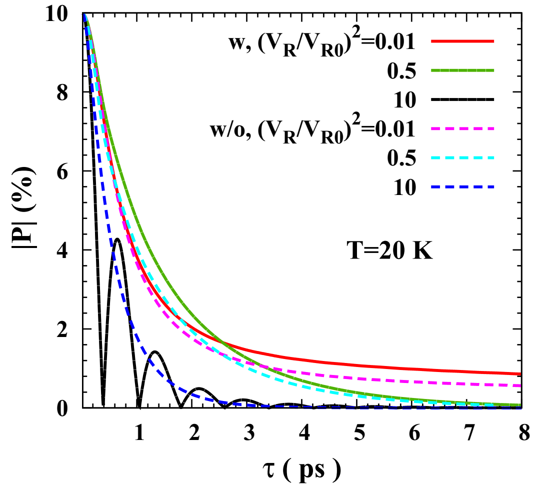

FIG. 7. Temporal evolution of the valley polarization in ML MoS$_2$ with (solid curves) and without (dashed curves) the off-diagonal elements in Eq. (A2). The role of the off-diagonal elements in the weak scattering $[(V/V_{R0})^2 = 0.01]$, EY-like $[(V/V_{R0})^2 = 0.5]$, and normal strong scattering $[(V/V_{R0})^2 = 10]$ regimes are shown.

matrix, the oscillation vanishes and the valley polarization becomes just the oscillation exponential decay (the blue dashed curve).

APPENDIX C: ANALYSIS ON THE EQUILIBRIUM STATE

We focus on the situation where the exchange energy is much smaller than the kinetic one. With the weak exchange interaction $\mathscr{H}^{\rm ex}_{\mathbf{k}}$, the delta function in Eq. (9) is expanded, e.g.,

$$\delta(E_{\mathbf{k}',+} - E_{\mathbf{k},+}) = \delta\big(\varepsilon_{\mathbf{k}'} - \varepsilon_{\mathbf{k}} + \varepsilon^{\rm ex}_{k'} - \varepsilon^{\rm ex}_{k}\big) \approx \delta(\varepsilon_{\mathbf{k}'} - \varepsilon_{\mathbf{k}}) + \frac{\partial\delta(\varepsilon_{\mathbf{k}'} - \varepsilon_{\mathbf{k}})}{\partial\varepsilon_{\mathbf{k}'}}\big(\varepsilon^{\rm ex}_{k'} - \varepsilon^{\rm ex}_{k}\big). \tag{C1}$$

With the linear order of the exchange energy retained in the scattering term [Eq. (9)], the KSBEs are written as

$$\frac{\partial\rho_{\mathbf{k}}}{\partial t} + \frac{i}{\hbar}[\mathscr{H}^{\rm ex}_{\mathbf{k}},\rho_{\mathbf{k}}] = \frac{2\pi}{\hbar}a^2\sum_{\mathbf{k}'}\delta(\varepsilon_{k'} - \varepsilon_k)(\rho_{\mathbf{k}'} - \rho_{\mathbf{k}}) + \frac{\pi}{\hbar}a^2\sum_{\mathbf{k}'}\frac{d\delta(\varepsilon_{k'} - \varepsilon_k)}{d\varepsilon_{k'}}\big\{\mathscr{H}^{\rm ex}_{\mathbf{k}} - \mathscr{H}^{\rm ex}_{\mathbf{k}'},\rho_{\mathbf{k}} - \rho_{\mathbf{k}'}\big\}. \tag{C2}$$

In the equilibrium state, $\partial_t\rho^e_{\mathbf{k}} = 0$ and $[\mathscr{H}^{\rm ex}_{\mathbf{k}},\rho^e_{\mathbf{k}}] = 0$. Hence, one obtains

$$\rho^e_{\mathbf{k}} = \rho^0_k + \int\frac{d\theta_{\mathbf{k}'}}{4\pi}d\delta(\varepsilon_{k'} - \varepsilon_k)\big\{\mathscr{H}^{\rm ex}_{\mathbf{k}} - \mathscr{H}^{\rm ex}_{\mathbf{k}'},\rho^e_{\mathbf{k}} - \rho^e_{\mathbf{k}'}\big\}. \tag{C3}$$

This integral equation can be approximately solved by using the iteration technique. It is assumed that $\rho^e_{\mathbf{k}} = B^0_k\hat{I} + \sum_{n=1}^{\infty}\rho^{(n)}_{\mathbf{k}}$. By substituting $B^0_k\hat{I} + \rho^{(1)}_{\mathbf{k}}$ on the left-hand side and $B^0_k\hat{I}$ on the right-hand side of Eq. (C3), one obtains $\rho^{(1)}_{\mathbf{k}} = \mathscr{H}^{\rm ex}_{\mathbf{k}}\partial B^0_k/\partial\varepsilon_k$. By repeating this process, one finds $\rho^{(2)}_{\mathbf{k}}$ is proportional to $(\varepsilon^{\rm ex}_k)^2$. Here, we only keep the linear order in the exchange energy, i.e.,

$$\rho^e_{\mathbf{k}} \approx B^0_k\hat{I} + \mathscr{H}^{\rm ex}_{\mathbf{k}}\partial B^0_k/\partial\varepsilon_k. \tag{C4}$$

Obviously, $\rho^e_{\mathbf{k}}$ commutes with $\mathscr{H}^{\rm ex}_{\mathbf{k}}$.

APPENDIX D: SOLUTION OF KSBEs WITH AN APPLIED FIELD

When the exchange interaction is weak, in the steady state ($\partial_t\rho_{\mathbf{k}} = 0$), the KSBEs with the external force field can be simplified to be

$$\frac{F}{\hbar}\frac{\partial\rho_{\mathbf{k}}}{\partial k_x} + \frac{i}{\hbar}[\mathscr{H}^{\rm ex}_{\mathbf{k}},\rho_{\mathbf{k}}] + \frac{1}{\tau}(\rho_{\mathbf{k}} - \rho^0_k) - \frac{1}{2\tau}\left\{\mathscr{H}^{\rm ex}_{\mathbf{k}},\frac{\partial\rho^0_k}{\partial\varepsilon_k}\right\} - \frac{\pi}{\tau}\int\frac{d\varepsilon_{k'}d\theta_{\mathbf{k}'}}{(2\pi)^2}\frac{d\delta(\varepsilon_{k'} - \varepsilon_k)}{d\varepsilon_{k'}}\{\mathscr{H}^{\rm ex}_{\mathbf{k}'},\rho_{\mathbf{k}'}\} = 0. \tag{D1}$$

Equation (D1) is an integral-differential equation, which can be solved by the iteration technique approximately. The density matrix is assumed to be $\rho_{\mathbf{k}} = \rho^e_{\mathbf{k}} + \sum_{n=1}^{\infty}\rho^{(n)}_{\mathbf{k}}$ with $\rho^{(n)}_{\mathbf{k}} \propto (\varepsilon^{\rm ex}_k)^n$.

The zeroth order of Eq. (D1) is exactly Eq. (C3), whose solution has been expressed by $\rho^e_{\mathbf{k}}$ [Eq. (24)]. The first order of Eq. (D1) reads

$$\rho^{(1)}_{\mathbf{k}} = -\frac{F\tau}{\hbar}\frac{\partial\rho^e_{\mathbf{k}}}{\partial k_x} = -\frac{F\tau}{\hbar}\frac{\partial}{\partial k_x}\left(B^0_k\hat{I} + \mathscr{H}^{\rm ex}_{\mathbf{k}}\frac{\partial B^0_k}{\partial\varepsilon_k}\right), \tag{D2}$$

which is just the drift form of the equilibrium state.

One notes that the drift density matrix $\rho^{(1)}_{\mathbf{k}}$ no longer commutes with $\mathscr{H}^{\rm ex}_{\mathbf{k}}$, which causes the precession of the "spin" vectors around the **k**-dependent effective magnetic field. The nth order ($n \geqslant 2$) density matrix satisfies

$$\frac{F}{\hbar}\frac{\partial\rho^{(n-1)}_{\mathbf{k}}}{\partial k_x} + \frac{i}{\hbar}[\mathscr{H}^{\rm ex}_{\mathbf{k}},\rho^{(n-1)}_{\mathbf{k}}] + \frac{1}{\tau}[\rho^{(n)}_{\mathbf{k}} - \bar{\rho}^{(n-1)}_{\mathbf{k}}] - \frac{1}{2\tau}\left\{\mathscr{H}^{\rm ex}_{\mathbf{k}},\frac{\partial\bar{\rho}^{(n-1)}_{\mathbf{k}}}{\partial\varepsilon_k}\right\} + \frac{1}{2\tau}\int\frac{d\theta_{\mathbf{k}'}}{2\pi}d\delta(\varepsilon_{k'} - \varepsilon_k) \times \{\mathscr{H}^{\rm ex}_{\mathbf{k}'},\rho^{(n-1)}_{\mathbf{k}'}\} = 0, \tag{D3}$$

where $\bar{\rho}^{(n)}_{\mathbf{k}} = 1/(2\pi)\int d\theta_{\mathbf{k}}\rho^{(n)}_{\mathbf{k}}$. Equation (D3) is complex, but fortunately it can be much simplified if only the density matrix in the linear order of F is retained (linear regime). Furthermore, $\bar{\rho}^{(n)}_{\mathbf{k}}$ ($n \geqslant 1$) and the last term on the left-hand side of Eq. (D3) are exactly zero due to the angle integration. Finally, one obtains ($n \geqslant 2$),

$$(i/\hbar)[\mathscr{H}^{\rm ex}_{\mathbf{k}},\rho^{(n-1)}_{\mathbf{k}}] + \rho^{(n)}_{\mathbf{k}}/\tau = 0. \tag{D4}$$

With $\rho^{(1)}_{\mathbf{k}}$ [Eq. (D2)] known, $\rho^{(n)}_{\mathbf{k}}$ ($n \geqslant 2$) can be obtained. By summing $\rho^{(n)}_{\mathbf{k}}$, one comes to a *closed* form of the density matrix for ML MoS$_2$ (for BL MoS$_2$, one replaces $\mathscr{H}^{\rm ex}_{\mathbf{k}}$ by $\tilde{\mathscr{H}}^{\rm ex}_{\mathbf{k}}$, and Ω_k by $\tilde{\Omega}_k$),

$$\rho_{\mathbf{k}} \approx \left(B^0_k\hat{I} + \mathscr{H}^{\rm ex}_{\mathbf{k}}\frac{\partial B^0_k}{\partial\varepsilon_k}\right) - \frac{F}{\hbar}\tau\frac{\partial B^0_k}{\partial k_x}\hat{I} + \frac{i}{\hbar^2}F\frac{\partial B^0_k}{\partial\varepsilon_k}\frac{\tau^2}{1 + 4\Omega^2_k\tau^2} \times \left[\mathscr{H}^{\rm ex}_{\mathbf{k}},\frac{\partial\mathscr{H}^{\rm ex}_{\mathbf{k}}}{\partial k_x}\right] - \frac{F}{\hbar}\frac{\partial\mathscr{H}^{\rm ex}_{\mathbf{k}}}{\partial k_x}\frac{\partial B^0_k}{\partial\varepsilon_k}\frac{\tau}{1 + 4\Omega^2_k\tau^2}. \tag{D5}$$

[1] K. F. Mak, C. G. Lee, J. Hone, J. Shan, and T. F. Heinz, Phys. Rev. Lett. **105**, 136805 (2010).
[2] A. Splendiani, L. Sun, Y. B. Zhang, T. S. Li, J. Kim, C. Y. Chim, G. Galli, and F. Wang, Nano Lett. **10**, 1271 (2010).
[3] D. Xiao, G. B. Liu, W. Feng, X. Xu, and W. Yao, Phys. Rev. Lett. **108**, 196802 (2012).
[4] X. D. Xu, W. Yao, D. Xiao, and T. F. Heinz, Nat. Phys. **10**, 343 (2014).
[5] H. Y. Yu, X. D. Cui, X. D. Xu, and W. Yao, Natl. Sci. Rev. **2**, 57 (2015).
[6] M. M. Glazov, E. L. Ivchenko, G. Wang, T. Amand, X. Marie, B. Urbaszek, and B. L. Liu, Phys. Status Solidi B **252**, 2349 (2015).
[7] T. Cao, G. Wang, W. Han, H. Ye, C. Zhu, J. Shi, Q. Niu, P. Tan, E. Wang, B. Liu, and J. Feng, Nat. Commun. **3**, 887 (2012).
[8] G. Sallen, L. Bouet, X. Marie, G. Wang, C. R. Zhu, W. P. Han, Y. Lu, P. H. Tan, T. Amand, B. L. Liu, and B. Urbaszek, Phys. Rev. B **86**, 081301(R) (2012).
[9] K. F. Mak, K. He, J. Sahn, and T. F. Heinz, Nat. Nanotech. **7**, 494 (2012).
[10] H. Zeng, J. Dai, W. Yao, D. Xiao, and X. Cui, Nat. Nanotech. **7**, 490 (2012).
[11] G. Wang, E. Palleau, T. Amand, S. Tongay, X. Marie, and B. Urbaszek, Appl. Phys. Lett. **106**, 112101 (2015).
[12] C. R. Zhu, K. Zhang, M. Glazov, B. Urbaszek, T. Amand, Z. W. Ji, B. L. Liu, and X. Marie, Phys. Rev. B **90**, 161302(R) (2014).
[13] G. Wang, X. Marie, I. Gerber, T. Amand, D. Lagarde, L. Bouet, M. Vidal, A. Balocchi, and B. Urbaszek, Phys. Rev. Lett. **114**, 097403 (2015).
[14] T. F. Yan, X. F. Qiao, P. H. Tan, and X. H. Zhang, arXiv:1502.07088.
[15] A. M. Zhang, J. H. Fan, Y. S. Li, J. T. Ji, G. H. Zhao, T. L. Xia, T. F. Yan, X. H. Zhang, W. Zhang, X. Q. Wang, and Q. M. Zhang, arXiv:1503.08631.
[16] B. R. Zhu, H. L. Zeng, J. F. Dai, Z. R. Gong, and X. D. Cui, Proc. Nat. Acad. Sci. **111**, 11606 (2014).
[17] B. R. Zhu, X. Chen, and X. D. Cui, Sci. Rep. **5**, 9218 (2015).
[18] G. Wang, X. Marie, L. Bouet, M. Vidal, A. Balocchi, T. Amand, D. Lagarde, and B. Urbaszek, Appl. Phys. Lett. **105**, 182105 (2014).
[19] A. M. Jones, H. Yu, J. S. Ross, P. Klement, N. J. Ghimire, J. Q. Yan, D. G. Mandrus, W. Yao, and X. D. Xu, Nat. Phys. **10**, 130 (2014).
[20] T. Olsen and I. Souza, Phys. Rev. B **92**, 125146 (2015).
[21] K. F. Mak, K. L. McGill, J. Park, and P. L. McEuen, Science **344**, 1489 (2014).
[22] J. Lee, K. F. Mak, and J. Shan, arXiv:1508.03068.
[23] H. Y. Yu, G. B. Liu, P. Gong, X. D. Xu, and W. Yao, Nat. Commun. **5**, 3876 (2014).
[24] C. Mai, A. Barrette, Y. Yu, Y. G. Semenov, K. W. Kim, L. Cao, and K. Gundogdu, Nano Lett. **14**, 202 (2014).
[25] Q. Wang, S. Ge, X. Li, J. Qiu, Y. Ji, J. Feng, and D. Sun, ACS Nano **7**, 11087 (2013).
[26] T. Yu and M. W. Wu, Phys. Rev. B **89**, 205303 (2014).
[27] M. M. Glazov, T. Amand, X. Marie, D. Lagarde, L. Bouet, and B. Urbaszek, Phys. Rev. B **89**, 201302 (2014).
[28] F. C. Wu, F. Y. Qu, and A. H. MacDonald, Phys. Rev. B **91**, 075310 (2015).
[29] Y. N. Gartstein, X. Li, and C. W. Zhang, Phys. Rev. B **92**, 075445 (2015).
[30] D. Y. Qiu, T. Cao, and S. G. Louie, Phys. Rev. Lett. **115**, 176801 (2015).
[31] M. Z. Maialle, E. A. de Andrada e Silva, and L. J. Sham, Phys. Rev. B **47**, 15776 (1993).
[32] A. Vinattieri, J. Shah, T. C. Damen, D. S. Kim, L. N. Pfeiffer, M. Z. Maialle, and L. J. Sham, Phys. Rev. B **50**, 10868 (1994).
[33] M. I. D'yakonov and V. I. Perel', Zh. Eksp. Teor. Fiz. **60**, 1954 (1971) [Sov. Phys. JETP **33**, 1053 (1971)].
[34] T. Yu and M. W. Wu, Phys. Rev. B **90**, 035437 (2014).
[35] A. Kumar and P. K. Ahluwalia, Phys. B: Condens. Matter **407**, 4627 (2012).
[36] J. Sinova, D. Culcer, Q. Niu, N. A. Sinitsyn, T. Jungwirth, and A. H. MacDonald, Phys. Rev. Lett. **92**, 126603 (2004).
[37] E. G. Mishchenko, A. V. Shytov, and B. I. Halperin, Phys. Rev. Lett. **93**, 226602 (2004).
[38] S. Murakami, Phys. Rev. B **69**, 241202(R) (2004).
[39] J.-i. Inoue, G. E. W. Bauer, and L. W. Molenkamp, Phys. Rev. B **70**, 041303(R) (2004).
[40] O. Chalaev and D. Loss, Phys. Rev. B **71**, 245318 (2005).
[41] O. V. Dimitrova, Phys. Rev. B **71**, 245327 (2005).
[42] S. Y. Liu, X. L. Lei, and N. J. M. Horing, Phys. Rev. B **73**, 035323 (2006).
[43] A. Khaetskii, Phys. Rev. B **73**, 115323 (2006).
[44] M. Glazov and A. Kavokin, J. Lumin. **125**, 118 (2007).
[45] K. Shen, R. Raimondi, and G. Vignale, Phys. Rev. B **90**, 245302 (2014).
[46] S.-i. Kuga, S. Murakami, and N. Nagaosa, Phys. Rev. B **78**, 205201 (2008).
[47] J. W. Wang and S. S. Li, Appl. Phys. Lett. **91**, 052104 (2007).
[48] W. Yao and Q. Niu, Phys. Rev. Lett. **101**, 106401 (2008).
[49] N. Nagaosa, J. Sinova, S. Onoda, A. H. MacDonald, and N. P. Ong, Rev. Mod. Phys. **82**, 1539 (2010).
[50] N. A. Sinitsyn, J. Phys.: Condens. Matter **20**, 023201 (2008).
[51] M. W. Wu, J. H. Jiang, and M. Q. Weng, Phys. Rep. **493**, 61 (2010).
[52] Y. Yafet, Phys. Rev. **85**, 478 (1952).
[53] R. J. Elliott, Phys. Rev. **96**, 266 (1954).
[54] *Semiconductor Spintronics and Quantum Computation*, edited by D. D. Awschalom, D. Loss, and N. Samarth (Springer, Berlin, 2002).
[55] I. Žutić, J. Fabian, and S. D. Sarma, Rev. Mod. Phys. **76**, 323 (2004).
[56] J. Fabian, A. M. Abiague, C. Ertler, P. Stano, and I. Žutić, Acta Phys. Slov. **57**, 565 (2007).
[57] *Spin Physics in Semiconductors*, edited by M. I. D'yakonov (Springer, Berlin, 2008).
[58] T. Korn, Phys. Rep. **494**, 415 (2010).
[59] V. Savona, C. Piermarocchi, A. Quattropani, F. Tassone, and P. Schwendimann, Phys. Rev. Lett. **78**, 4470 (1997).
[60] V. Savona, J. Phys.: Condens. Matter **19**, 295208 (2007).
[61] L. Wang and M. W. Wu, Phys. Lett. A **378**, 1336 (2014); Phys. Rev. B **89**, 115302 (2014).
[62] L. Wang and M. W. Wu, Phys. Rev. B **89**, 205401 (2014).
[63] F. Yang, L. Wang, and M. W. Wu, Phys. Rev. B **92**, 155414 (2015).
[64] T. Cheiwchanchamnangij and W. R. L. Lambrecht, Phys. Rev. B **85**, 205302 (2012).
[65] W. Jin, P.-C. Yeh, N. Zaki, D. Zhang, J. T. Sadowski, A. Al-Mahboob, A. M. van der Zande, D. A. Chenet, J. I. Dadap,

I. P. Herman, P. Sutter, J. Hone, and R. M. Osgood, Jr., Phys. Rev. Lett. **111**, 106801 (2013).

[66] W. Jin, P. C. Yeh, N. Zaki, D. Zhang, J. T. Liou, J. T. Sadowski, A. Barinov, M. Yablonskikh, J. I. Dadap, P. Sutter, I. P. Herman, and R. M. Osgood, Jr., Phys. Rev. B **91**, 121409 (2015).

[67] J. L. Cheng and M. W. Wu, J. Appl. Phys. **99**, 083704 (2006).

[68] P. Zhang and M. W. Wu, Phys. Rev. B **84**, 045304 (2011).

[69] T. Kuhn and F. Rossi, Phys. Rev. Lett. **69**, 977 (1992).

[70] H. Haug and A. P. Jauho, *Quantum Kinetics in Transport and Optics of Semiconductors* (Springer, Berlin, 1996).

[71] M. W. Wu and H. Metiu, Phys. Rev. B **61**, 2945 (2000).

[72] M. W. Wu and C. Z. Ning, Eur. Phys. J. B **18**, 373 (2000); Phys. Status Solidi B **222**, 523 (2000).

[73] N. S. Averkiev and M. M. Glazov, Semiconductors **42**, 958 (2008).